RECENT CLUSTER WIDEBAND STUDIES OF AURORAL KILOMETRIC RADIATION

R. Mutel[(1)], D. Menietti[(1)], I. Christopher[(1)], D. Gurnett[(1)], J. Cook[(1)], and H. Frey[(2)]

(1) Dept. Physics & Astronomy, Univ. Iowa, Iowa City, IA, 52242, USA, Emails: robert-mutel@uiowa.edu, jdm@space.physics.uiowa.edu, ivar-christopher@uiowa.edu, donald-gurnett@uiowa.edu , Justin-cook2@uiowa.edu

(2) Space Science Lab, U. C. Berkeley, Berkeley, CA, 94720,USA, Email: hfrey@ssl.berkeley.edu

ABSTRACT

We report on two recent studies of auroral kilometric radiation (AKR) using the Cluster WBD instrument. The first study involves a statistical investigation of a distinct type of AKR fine structure called striated AKR (SAKR). We find that the unique characteristics of SAKR (temporal signature, slope magnitude and sign, extremely narrow bandwidths, beam angular sizes) are all consistent with triggering by upward travelling ion solitary structures (a.k.a. 'ion holes'). We calculate the expected perturbation of a horseshoe electron distribution function by an ion hole. We integrate the resonance condition for a cyclotron maser instability (CMI) using the perturbed velocity distribution. We find that the CMI growth rate can be strongly enhanced as the horseshoe velocity distribution contracts inside the passing ion hole, resulting in a power gain increase greater than 80 dB. The gain curve is sharply peaked just above the R-X-mode cut-off frequency, with an effective bandwidth $\leq$50 Hz, consistent with the observed bandwidth of SAKR emission. Ion holes, as observed *in situ* in the acceleration region, are detected primarily in the upward current region, move upward, and have speeds (50-400 km s^{-1}) consistent with the observed slopes of SAKR bursts. Hence, we suggest that SAKR bursts are a remote sensor of ion holes and can be used to determine the frequency of occurrence, locations in the acceleration region, and temporal characteristic of these structures.

The second study involves comparing AKR source locations, determined using VLBI differential delay mapping, with contemporaneous UV imaging of the auroral oval in the same hemisphere. This provides a new opportunity to study magnetospheric-ionospheric coupling by investigating the correspondence between AKR source region conditions and auroral precipitation physics on the same magnetic field lines. Initial results indicate that there is good correlation between the AKR burst locations and bright features on the same magnetic field line in the auroral oval. However, detailed comparison with high time resolution (1-2 min) indicates that short time-scale AKR bursts and auroral brightenings may not be well correlated.

These early results are tentative and based on only a few epochs. The joint WBD-IMAGE observing program is now in its most intensive observing phase (mid-2005 through 2006).

1. STRIATED AKR (SAKR): A TRACER OF ION HOLES?

1.1 Observed properties of SAKR

Auroral kilometric radiation (AKR) bursts exhibit a bewildering variety of fine structure as seen on frequency-time spectra (Fig. 1). Wu and Lee [41] have no doubt correctly identified the electron cyclotron maser instability as the plasma mechanism responsible for the emission, but as pointed out some years ago by Melrose [21], this mechanism would be an incomplete theory if it could not explain the time scales of wave growth associated with AKR fine structure. Gurnett et al. [15] first suggested that the drifting features may be due to rising and falling source regions along an auroral magnetic field, with frequency equal to the local electron cyclotron frequency. The fine structures, illustrated in Fig. 1, include not only slowly drifting features (labelled A, B), but also discrete striated quasi-periodic bands of nearly monochromatic emission with negative frequency slopes (Fig. 1, label C). We will refer to this emission as SAKR (striated AKR)

Occurrence frequency

AKR emission is frequently detected, especially during sub-storm onset. The occurrence probability of AKR is nearly 30% for geomagnetic index K_p in the range $1 < K_p < 3$, with the highest occurrence frequency in the winter polar regions [19]. By contrast, the occurrence frequency of SAKR emission is quite low. We detect SAKR bursts with the Cluster wideband (WBD) plasma instrument [16] in less than 1% of all spectra. There is a strong inverse correlation with observing frequency, with most detections in the 125-135 kHz band [Fig 2]. Menietti et al. [23,24] also studied SAKR emission using the plasma wave instrument (PWI) receiver on the Polar spacecraft. They also found an inverse correlation with observing frequency, with a 6% detection rate in the 90 kHz band.
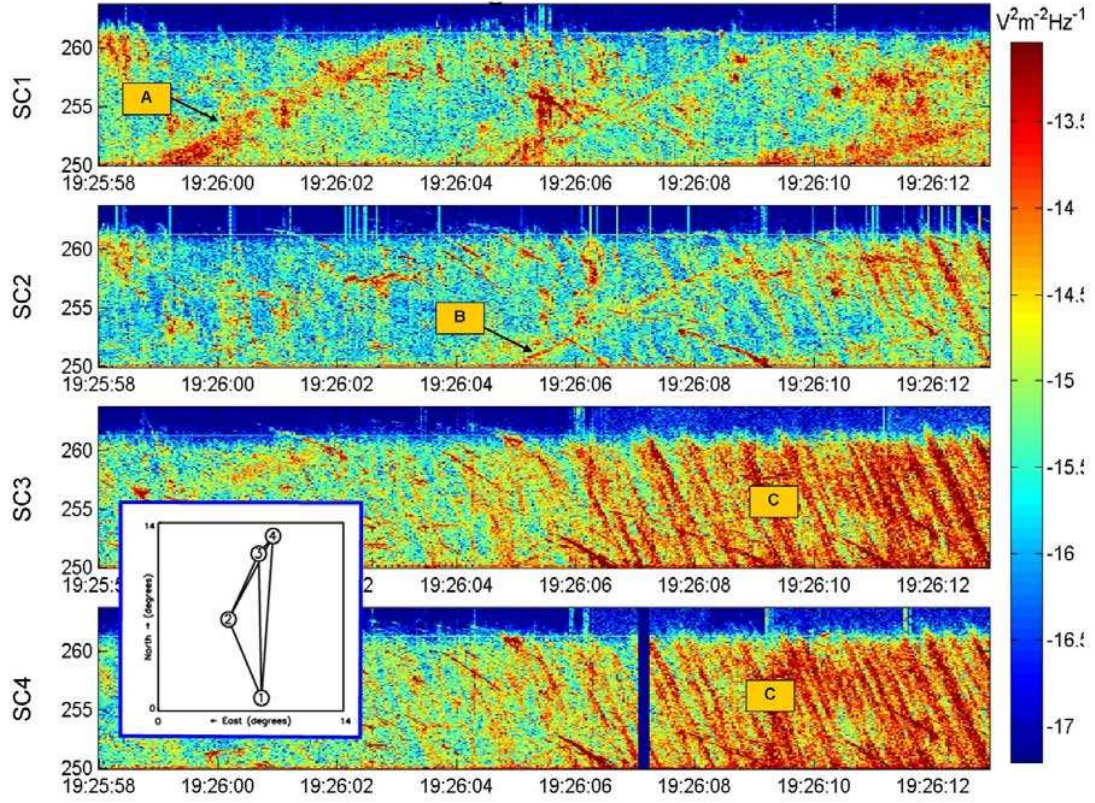
Fig 1. Cluster 4-spacecraft WBD frequency-time spectra of AKR bursts during an active period. Slowly drifting, positive slope AKR bursts are often seen (A), as are narrower bursts (B). The much rarer quasi-periodic very narrowband striated (SAKR) bursts (C) are hypothesized to be triggered by upward travelling solitary structures. Inset shows spacecraft angular separation as seen from AKR source region. Note the narrow illumination beam of SAKR (SC 3 and 4 are only separated by 1.5°; the SAKR bursts are barely detected on SC2, undetected on SC1).
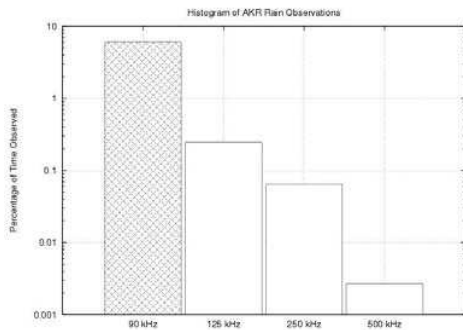

Fig. 2. Frequency of occurrence of SAKR bursts as a function of observing frequency. The data at 90 kHz (hatched bar) is from [24].

Frequency drift and speed

SAKR bursts have negatively sloped, nearly linear morphologies, at least within the 10 KHz wide bandwidth of the WBD receivers. The majority of the slopes range between -2 kHz s^{-1} and -8 kHz s^{-1}. Assuming the emission frequency is identified with the local electron cyclotron frequency, the speed of the stimulator as a function of frequency and slope can be written

$$V = 540 \frac{km}{s} \cdot \left(\frac{\alpha}{10\,kHz/s} \right) \left(\frac{100\,kHz}{f} \right)^{\frac{4}{3}} (1)$$

where V is the stimulator speed (km s^{-1}), α is the observed slope of the SAKR burst (kHz s^{-1}) and f is the observed frequency (kHz). Figure 3 shows a histogram of the observed slopes of 650 SAKR burst events observed in the 125-135 kHz band along with the derived trigger speeds (top x axis). The mean slope is -5.6 kHz s^{-1}, with more than 90% of the slopes in the range -2 to -8 kHz s^{-1}. The corresponding trigger speeds, using equation 1, are in the range 76 – 303 km s^{-1}, with a mean value 213 km s^{-1}. These results are similar to those reported by Menietti et al [24] who found that the SAKR

slope magnitude measured with the Polar WBR instrument increased with frequency, from -4.4 kHz s^{-1} (349 km s^{-1}) at 75 kHz to -5.7 kHz s^{-1} (152 km s^{-1}) at 170 kHz.
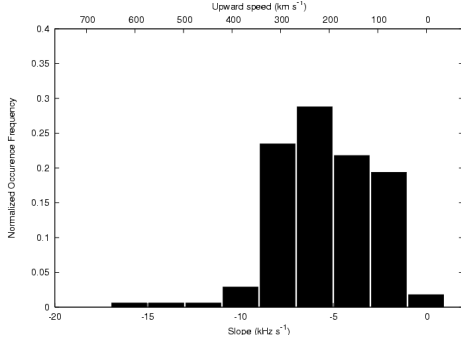

Fig 3. Histogram of observed SAKR burst slopes in the 125-135 kHz band (bottom axis) and derived trigger speed (top axis, from equation 1) of the trigger event.

Bandwidth

One of the most unusual features of SAKR bursts is their extraordinarily narrow bandwidth. The top panel of figure 4 shows a single isolated SAKR burst. The middle panel shows the same feature, but after de-trending by subtraction of a 'chirp' signal of best-fit constant negative slope. The lower panel shows the full width at half maximum of a Gaussian function fit along the frequency axis of the de-trended signal after summing in time intervals of 37 ms each. The resulting bandwidths, in the range 15 – 22 Hz, are much narrower than previously reported either observationally [e.g. 15] or resulting from model calculation of AKR emission [e.g. 36, 42] although Baumback and Calvert [1] also reported AKR bandwidths as small as 5 Hz. (In the latter paper, the spectrograms do not appear to be SAKR emission). Other SAKR bursts we have examined have bandwidths ranging from 15 to 40 Hz.

The narrow bandwidth implies a small source extent along the z (B-field) direction, viz,

$$\Delta z = 2.5\, km \cdot \left[\frac{100\, kHz}{f} \right]^{\frac{4}{3}} \left[\frac{\Delta f}{kHz} \right] \quad (2)$$

where Δz is the source extent along the B field, Δf is the observed bandwidth, and Re is the Earth's radius. For f = 130 KHz and Δf = 20 Hz we obtain Δz = 0.76 km. This is considerably smaller than the lateral extent of the AKR source region and indicates the trigger for SAKR must have a z-dimension of order ~1 km.
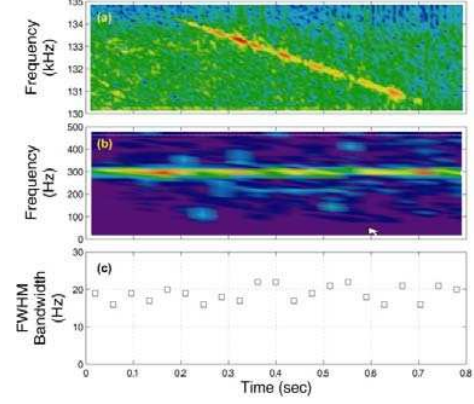

Fig 4. SAKR bandwidth. (a) SAKR burst observed with Cluster WBD, (b) Same burst, but detrended, (c) Measured bandwidth in 37 ms intervals.

Angular Beam Size and average source power

The WBD instrument on the Cluster constellation has the unique ability to simultaneously sample the flux density of individual AKR bursts at four widely separated points in space. By comparing the flux density on pairs of spacecraft, we can estimate the average angular beam size of individual bursts. The beaming probability is defined using the following algorithm. For each pair of spacecraft during a given observation, we calculate the projected angular separation between spacecraft as seen from a location situated above the magnetic pole of the hemisphere being observed, at a height corresponding to the electron cyclotron frequency at the mid-observing band (e.g. 2.35 R_e for the 125 kHz band). This constitutes an average AKR location in that band without regard to location on the auroral oval. We then divide the time-frequency spectrum from each spacecraft pair (50 sec duration for 125 kHz band) into data 'cells' 300 ms x 1 kHz in size. The intensities are normalized to correct for differing distances between individual spacecraft and the AKR source. We then omit from further analysis all data cells whose intensities are below a threshold, arbitrarily chosen to be 10 dB above the noise flow of that spectrum. Finally, we compare intensities in each pair of data windows, assigning a weight 1 to pairs for which the intensities are within 10 dB of each other, and 0 otherwise. The overall beaming probability for each angular separation interval is the sum of the beaming weights divided by all cell pairs.

Note that this scheme is susceptible to overestimation of the beaming probability, since it is possible that independent AKR sources will illuminate separate spacecraft at the same frequency and time interval. This 'confusion' problem is smaller for SAKR emission since it is often clear from the burst morphology on a time-

frequency spectrum that only one source contributes to a given data cell at one time, whereas with normal AKR there are very often several intersecting, drifting sources which contribute to a given data cell (cf. fig 1).

In fig 5 we plot the beaming probability versus angular separation for 651 SAKR bursts in the 125-135 kHz and 250-260 kHz bands. We have fitted a Gaussian function to the 125 kHz band observations using a least-squares fitting algorithm. The resulting full width at half maximum (FWHM) angular size is $\theta = 4.5°$ (solid angle $\Omega = 0.006$sr). This is surprisingly small compared with most previously published observations of AKR beam size e.g. Green and Gallagher [13], who reported beaming solid angles of 4.6sr and 3.3sr at 178 and 100 KHz respectively. They made angular beaming estimates by comparing time-averaged spectra
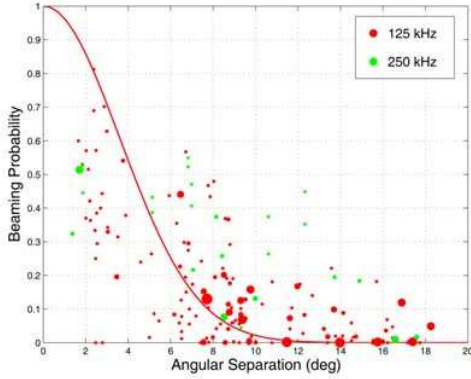

Figure 1 Angular beamsize probability for elementary radiation sources [ERS] measured using multiple Cluster spacecraft for 651 SAKR bursts observed in the 125 and 250 KHz bands

observed using two satellites (Hawkeye and IMP-6) which simultaneously observed AKR bursts while the spacecraft were both over the same polar region. Since the time resolution used for the Hawkeye-IMP6 spectrum comparison (several minutes) far exceeds the time-scale of individual AKR bursts, their measured angular beam is actually a measure of the ensemble-averaged sky distribution of AKR bursts over a several minute time-scale rather than the angular beam size of individual AKR emission sources. This is the confusion problem mentioned above.

The angular beaming observations allow a direct estimate of the average intrinsic power of individual SAKR bursts. We calculate the average power for intense bursts, such as those labelled C in fig. 1. The typical flux density received of an intense SAKR burst, such as those illustrated in fig. 1, is $S_\nu \sim (1\text{-}10) \times 10^{-13}$ V^2 m^{-2} Hz^{-1} at a source-

spacecraft distance d = 10R$_e$. The power emitted at the AKR source is

$$P = 4\pi d^2 \cdot \frac{S_\nu}{Z_0} \cdot \Delta\nu \cdot \frac{\Omega}{4\pi} \qquad (3)$$

where $Z_0 = 377$ ohms is the impedance of free space, $\Delta\nu \sim 20\text{-}50$ Hz is the bandwidth of a burst, and $\Omega \sim 0.006$ sr, is the solid angle of the emission beam. The resulting power is P $\sim$ 1 – 10 W, much smaller than the commonly accepted values P $\sim$ 10^3-10^4 W for 'elementary radiation events' [33].

1.2 Connection with ion holes

Summary of observed properties of ion holes

Ion holes (a.k.a. ion solitary structures) are small-scale (1-2 km) depletions in ion density associated with upgoing ion beams. They are seen in spacecraft electric field measurements as symmetric bipolar parallel electric field structures with amplitudes 10 – 500 mV m^{-1} and timescales 3-10 ms. They were first detected in S3-3 spacecraft observations [40] and have been studied using in situ measurements in the acceleration region by several authors [e.g. 3, 8, 20]. Ion holes travel upward at measured speeds between 75-300 km s^{-1} [3, 8], although McFadden et al. [20] argue for somewhat higher speeds, in the range 550- 1100 km s^{-1}. The width of the waves increase with amplitude [8] which is inconsistent with small amplitude 1-d soliton models, but which supports a BGK-type generation mode [25].

Electron distribution function and CMI growth rate

The free energy for AKR radiation arises from wave growth resulting from the interaction of a radiation field with an electron velocity distribution having a positive slope in the direction perpendicular to the magnetic field ($\partial f/\partial v_\perp > 0$). The condition for waves of angular frequency ω and wave normal angle θ to resonate with electrons with angular frequency ω_{ce} and velocity v is given by [41]

$$k_\parallel v\cos\theta - \omega + n\frac{\omega_{ce}}{\gamma\left(v_\parallel, v_\perp\right)} = 0 \qquad (4)$$

where ω_{ce} is the electron cyclotron frequency, n is an integer, and γ is the Lorentz factor of the relativistic electrons. The cyclotron maser instability (CMI) is the case $n = 1$. If we assume that the electrons are mildly relativistic, as is observed in the AKR source region (E$_e \sim$ 10 keV, so $\gamma \sim$1.01), we can expand the Lorentz factor to obtain the equation for a circle in velocity space

$$v_\perp^2 + \left(v_\parallel - v_{\parallel c}\right)^2 = v_r^2 \qquad (5)$$

where the resonant circle's center is on the horizontal axis displaced by

$$v_{\parallel c} = \frac{k_\parallel}{\omega_{ce}} c^2 \qquad (6)$$

and the radius of the resonant circle is

$$v_r = v_{\parallel c} \left[1 - \frac{2c^2\left(\omega - \omega_{ce}\right)}{\omega_{ce} v_{\parallel c}^2}\right]^{\frac{1}{2}} \qquad (7)$$

Analysis of recent FAST observations of AKR emission in the source region [9,11,36] provides evidence that the AKR k-vector direction at the source is nearly perpendicular to the B field ($k_\parallel \sim$ 0). This is based on observations of wave polarization in the source region. The E-field of the wave is polarized perpendicular to the ambient magnetic field which indicates that the wave is purely X-mode [39]. In the following, we explicitly assume $k_\parallel = 0$, so that the radius of the resonance circle becomes

$$v_r = c \left(\frac{2\delta\omega}{\omega_{ce}}\right)^{\frac{1}{2}} \qquad (8)$$

where $\delta\omega = \omega_{ce} - \omega$. The gain of CMI mechanism is given by calculating the imaginary part of the angular frequency ω

$$\omega_i = \frac{\pi^2 \omega_{pe}^2 \omega_{ce}}{4\omega n_e} \oint dv_\perp v_\perp^2 \frac{\partial f}{\partial v_\perp} \qquad (9)$$

where the $v_\perp$ integral is performed on the closed circular path given by equation 4.

The electron velocity distribution in the upward current acceleration region has been measured *in situ* by FAST [7]. It consists of an incomplete shell or 'horseshoe' shape in velocity space. We have modelled the observed velocity distribution using a simple analytic functional form

$$f(v) = g(v) e^{-\left(\frac{v - v_0}{\Delta}\right)^2} \qquad (10)$$

where Δ is the horseshoe width, v_0 the horseshoe radius and the loss-cone function g is

$$g(v) = 1 - \beta \cdot \mathrm{sech}\left(\frac{\tan^{-1}\left(v_y / v_x\right)}{\Theta}\right) \qquad (11)$$

where β is a dimensionless scaling factor and Θ is the characteristic width of the loss cone. The model velocity distribution function is shown in figure 6 along with a measured velocity distribution function from FAST [11].
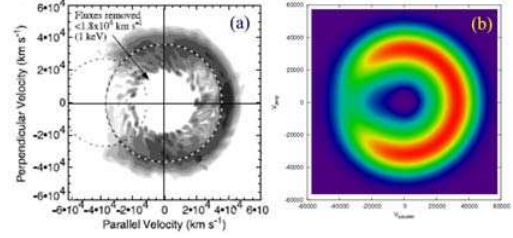

Fig. 6. (a) Electron distribution function measured by FAST in AKR source region (from ref [11], fig. 3a). (b) Model distribution.
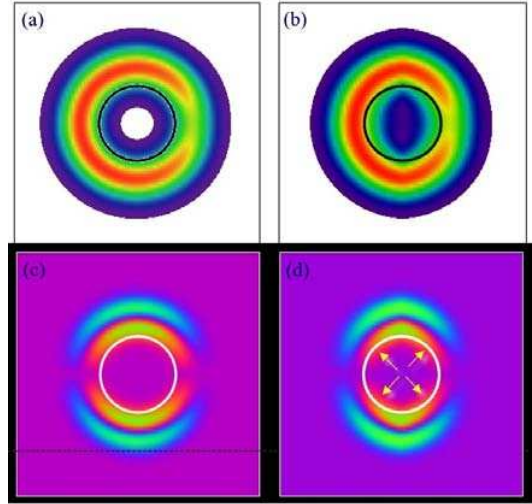

Fig. 7. Top panel: horseshoe electron velocity distribution function outside ion hole (*a*), and inside ion hole (*b*). Black circle is the CMI resonant circle. The $v_{//}$ direction is the horizontal axis, Earthward to left. Bottom panel: weighted partial derivative $\partial f/\partial v_\perp$ outside ion hole (*c*), and inside ion hole (*d*). The arrows indicate the parts of the growth line integral (equation 9) most enhanced inside the ion hole.
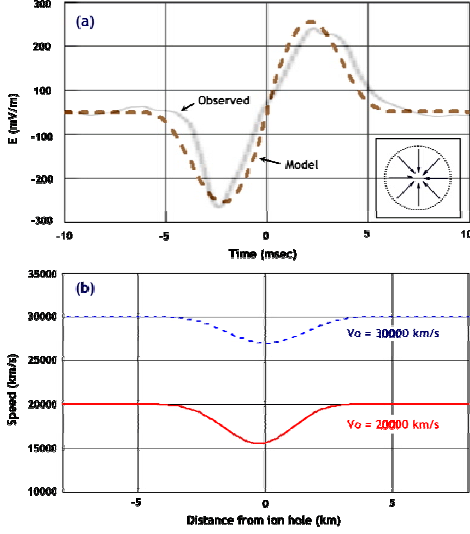
Fig 8. (a) Observed electric field vs. time (solid line) as an ion hole passes by FAST spacecraft [20, fig. 10], and best-fit model (dashed line) using equation (12). The inset at lower right shows a simple spherical model of an ion hole with inward electric field. (b) Calculated parallel velocity vs. distance from an ion hole for an electron passing through the hole with an impact parameter 1 km and initial velocities 20,000 km s^{-1} (dotted line) and 30,000 km s^{-1} (solid line). The assumed hole speed is 300 km s^{-1}.

Triggering SAKR emission by an ion hole

A passing ion hole will briefly perturb the electron distribution function. Since the electrons are magnetized (cyclotron radius $r_{ce}\sim$50m, much smaller than the ion hole parallel scale size $L_{ih} \sim 1$ km), the effect on the perpendicular velocity component is negligible (a small **E**x**B** drift, $V_D \sim 40$ m s^{-1}). However, the parallel velocity will experience a significant decrease as the electrons 'climb' the potential well of the hole. To determine the magnitude of the effect, we have modelled the observed electric field structure of an ion hole using the analytic form

$$E(t) = E_0 \tanh\left(\frac{t}{\tau}\right)\sec h\left[\frac{t}{\tau}\right] \quad (12)$$

Figure 8a shows an observed E-field of an ion hole [20, fig. 10] along with a plot of the model (equation 12, $E_0 = 500$ mV m^{-1}, $\tau = 2$ ms).

We used this model to calculate the velocities of electrons as they traverse the hole for a variety of impact parameters and initial speeds. For initial parallel speeds of 20,000 and 30,000 km s^{-1} (cf. fig. 6), the speed of an electron traversing an ion hole at a minimum distance of 1 km from the center is

shown in figure 8b. As expected, the parallel velocity briefly decreases, so that the horseshoe velocity distribution is 'squeezed' on the parallel (horizontal) axis, as shown in figure 7b. The speed decrease is proportional to v^{-1} as expected by a simple energy conservation argument: For an electric field E and hole diameter L_{ih}, the potential well of the ion hole is approximately $\Phi \sim E \cdot L_{ih}$. The electron loses kinetic energy as it 'climbs' the potential well so that energy conservation requires

$$\delta\left(\frac{1}{2}mv_{\parallel}^{2} + q_e\Phi\right) = 0 \qquad (13)$$

Solving for the velocity change,

$$\delta v_{\parallel} = \frac{q_e\delta\Phi}{m_e v_{\parallel}} \qquad (14)$$

For an ion hole electric field E $\sim$ 300 mV m^{-1}, diameter $L_{ih} \sim 2$ km, and $v_0 = 20,000$ km s^{-1}, the expected speed decrease is $\delta v \sim 5,000$ km s^{-1}, in good agreement with the detailed calculation. The resulting CMI growth rate for the unperturbed and perturbed velocity distribution is shown in figure 9.
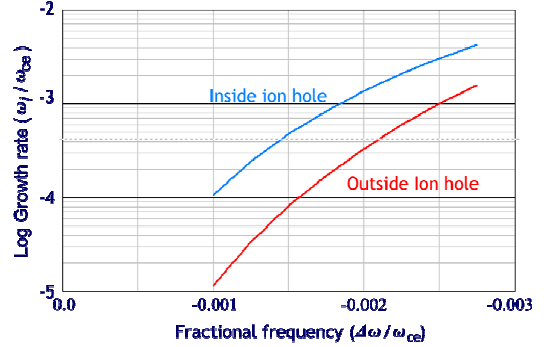

Figure 9. Growth rate as a function of fractional frequency.

In order to calculate the power gain in the perturbed region, we need an estimate of the convective growth length

$$L_c = \frac{V_g}{|\omega_i|} \qquad (15)$$

where V_g is the group velocity of the wave and ω_i is the growth rate. The group velocity is very sensitive to the ratio of plasma to cyclotron frequency and the detailed velocity distribution function. As a first approximation, we have used the cold plasma dispersion relations to estimate the group velocity $Vg = d\omega/dk$ for frequencies near the R-mode cut-off frequency. We find that Vg is of order 1,000 km s^{-1}. This is similar to the estimate used by Omidi

and Gurnett [28], but significantly lower than that of Pritchett et al. [36].

For a maximum growth rate $\omega_i \sim 5000$ s^{-1} (figure 9), the corresponding convective growth length is $L_c \sim$ 200m Hence, there are approximately 5-10 e-folding lengths in the region of the hole, assuming a perpendicular physical scale of order 1-2 km. This results in a maximum power gain of $e^{10-20} \sim$ 43-87 dB. The power gain required to amplify the background radiation to observed levels of normal (wideband) AKR was estimated by Omidi and Gurnett [28] to be e^{20}, which is at the high end of our calculation. However, as discussed above, since SAKR emission is highly beamed, the power is a factor of ~100 smaller, so the required power gain is closer to $e^{15} = 65$ dB. This is comfortably within the range predicted by an ion hole trigger.

In Figure 10 we plot the power gain (dB) as function of frequency for f_{ce} =128 kHz (2.35 Re), a convective path Lc = 100m, an effective hole width of 1 km, and a horseshoe velocity distribution with a mean energy E = 7 keV. (Note that there is also gain outside the hole, but since it is ~60 dB below the peak level, it is not detectable). The gain reaches 90 dB, but the gain curve is highly peaked very near the X-mode cut-off frequency. If we estimate the dynamic range of SAKR bursts at 10-20 dB (e.g. Fig. 1), the effective bandwidth is the frequency range from the peak to ~20 dB below the peak. From the gain plot (fig. 10), the corresponding frequency interval is $\Delta f \sim 40$ Hz (shaded region), in good agreement with the measured bandwidth of SAKR (fig. 4).

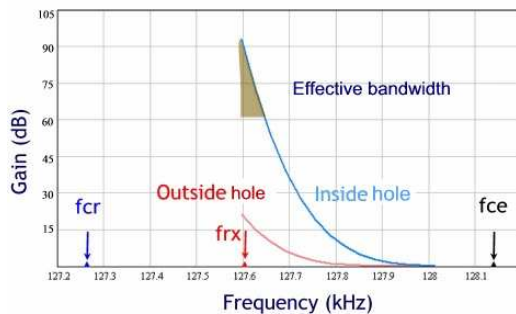Figure 10. CMI gain in decibels vs. escaping frequency for a sample case f_{ce} = 128 kHz (2.35R$_e$), Lc = 100 m, and mean kinetic energy 7 keV. The electron cyclotron frequency (f_{ce}), R-mode cut-off frequency (f_R), and relativistic cyclotron frequency (f_{cr}) are marked. The shaded triangle indicates the effective frequency range for which the gain is above the minimum detection threshold.

1.3 Ion holes, Electron holes, and Tri-polar structures

Pottelette and colleagues [33-35] have proposed that electron holes or 'tri-polar structures' (electron holes contained within ion holes), rather than ion holes, are the cause of AKR drifting fine structure. While some AKR fine structure may indeed by associated with electron holes and/or tri-polar structures, we find that the observed properties of ion holes provide a better match to SAKR burst characteristics for the following reasons.

1. *Location*. Electron holes have been observed regularly in the downward current region of the magnetosphere, but only once in the upward current region [20]. By contrast, ion holes are found regularly in the upward current region [3,8,20,40], which is the source region of AKR [9]. On the other hand, Pottelette and Treumann [35] show a FAST VLF waveform with a quasi-periodic chain of tri-polar structures in the auroral acceleration region, very similar to the SAKR burst intervals. It is not yet clear how common tri-polar structures are in the acceleration region compared with ion holes.

2. *Speed*. Ion holes are observed moving upward (e.g., [3]) in the AKR source (upward current) region, in agreement both with SAKR burst negative slopes. This is also consistent with simulations, which predict that ion holes should move in the direction of the ion beam at a fraction of the beam speed (e.g. [6]). Ion holes have observed speeds compatible with the speeds derived from slopes of SAKR bursts (75-300 km/s) [3,8], although McFadden et al. [20] report somewhat higher speeds. However, the derived speeds do not match the observed speeds of electron holes which are typically much higher, 500 - 5000 km s^{-1} [3,5,10]. Less is known about the speed of tri-polar holes. Pickett et al. [32] used time delays between Cluster spacecraft located above the auroral zone near 6 R$_E$ to estimate the speeds of several tri-polar holes. They deduced speeds of 'several hundred to a few thousand km/s'. While this is too high to explain the majority of SAKR burst slopes, the speeds of tri-polar structures lower in the auroral acceleration region may be different.

Pottelette and Treumann [35] argue that tri-polar structures arise in the vicinity of double layers with large amplitudes, as seen in the simulations of Goldman et al. [12]. They argue that a typical hole speed will be the difference between the bulk ion beam speed and the local ion acoustic speed, typically tens of km/s upward, although the holes could drift either upward or downward depending on the sign of the difference. This is not in agreement with SAKR slopes, which are always negative (upward trigger), but could explain other

types of narrowband AKR bursts, which are observed to drift in both directions.

3. *Energetics.* Pottelette et al. [33] have discussed the production of narrow-band AKR emission resulting from perturbation of the electron velocity distribution by electron holes. However, it is a heuristic approach and the growth rate determined from the CMI resonant integral over the perturbed distribution is not described in detail. Hence, it is difficult to compare the growth efficiency with that of an ion hole as described above. However, Bounds et al. [3] found that the peak potential of electron holes in the acceleration region was significantly (2x-3x) smaller than that of ion

holes, so that one expects an average ion hole to

have a larger effect on the ambient electron distribution. For tri-polar holes, we have modelled the expected perturbation of ambient electron velocity distribution function by a tri-polar hole using the same scheme as described above. We used an E-field signature similar to that shown in Fig. 2 of Pottelette and Treumann [34]. We find that the maximum perturbation of the parallel velocity is significantly smaller (e.g. 10% reduction vs. 25% for ion hole), as could be expected, since the electrons see alternating acceleration and deceleration rather than a single potential 'hill'. We have not yet calculated the resulting CMI growth rates, but they can be expected to be much smaller than those for ion holes with the same peak E-field.
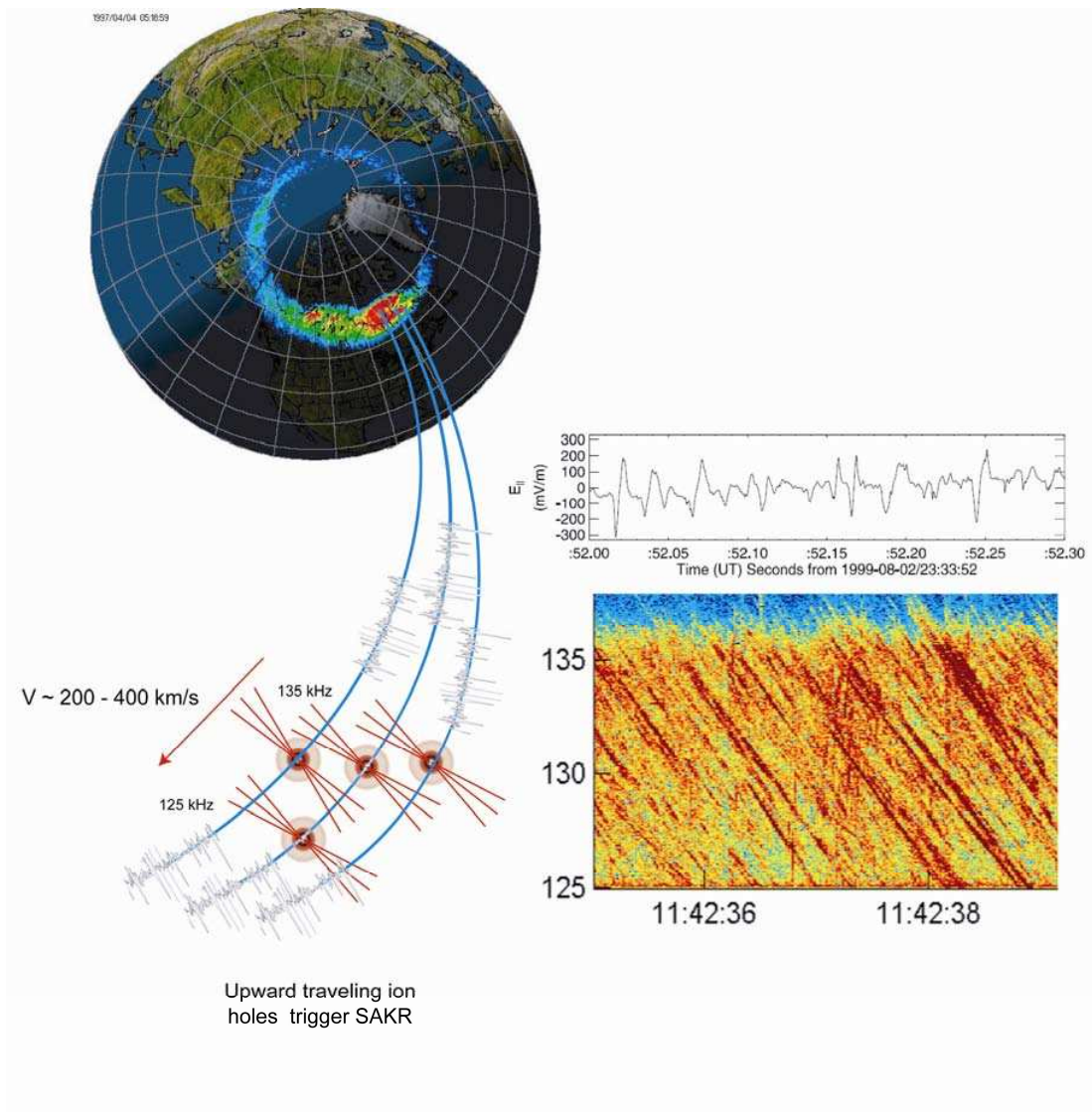

Figure 11. Cartoon illustrating triggering of SAKR bursts by trains of ion holes.

2. THE AKR-AURORA CONNECTION: SIMULTANEOUS OBSERVATIONS OF AKR AND AURORAL ARC LOCATIONS

2.1 Summary of Previous AKR-Auroral Correlative Studies

It is now well established that auroral kilometric radiation (AKR) is generated on auroral field lines in regions of depleted electron density above the auroral zone. The location of the AKR emission was first investigated by Gurnett [14] in 1974, who noted that the time of receipt of AKR bursts were consistent with source locations along auroral field lines near the Earth (R < 3 Re). Gurnett also found that the probability of intense AKR bursts was closely correlated with discrete auroral arcs in the local evening region of the auroral zone, although the AKR-auroral correlation was temporal and not positional.

The next year, Kurth et al. [18] strengthened the AKR-auroral connection by comparing AKR source positions obtained from antenna null measurements on Hawkeye I and Imp 8 with simultaneous optical images of the northern auroral zone from the DAPP satellite. They presented two cases in which the most intense emission occurred on field lines above discrete arcs seen on the DAPP auroral images. In a more systematic study, Benson and Akasofu [2] compared 38 epochs of AKR observations obtained from the ISIS 1 spacecraft with visual observations from a network of Alaskan all-sky cameras. In general, intense AKR was associated with bright auroral arcs, and weak or undetected AKR corresponded to times with no aurora or only a faint arc or weak diffuse aurora. The correlation was strictly temporal, since no location information was available for the AKR bursts.

Calvert [4] developed a direction-finding technique using the relative phase of orthogonal antennas to determine AKR source directions, which was later used by Huff et al. *[17]* to find the locations of several strong AKR bursts at several frequencies. Assuming that the radiation arises from cyclotron resonant altitudes, they found that the inferred locations were on field lines connected to bright spots on optical auroral images taken concurrently with the DE-1 satellite. Pederson et al. [31] reported on two joint AKR-auroral events involving 'transpolar' or theta auroral arcs. They compared AKR observations from the HF wave experiment with the UV imaging instrument, both on the Viking satellite. The AKR source locations were assumed to be at or near the spacecraft position when the emission frequency was nearly the same as the measured electron cyclotron frequency. During these times, the field line intersecting the satellite connected to transpolar arcs visible in the UV images.

Recently, Panchenko [29] described a 3-antenna AKR location scheme which provides instantaneous burst location with a typical directional uncertainty ± 6° in latitude and ± 12° in MLT. He compares the derived location of an AKR burst observed with the Interball-2 satellite with a simultaneous UV image from POLAR and finds excellent positional agreement.

2.2 WBD-VLBI AKR location technique

We have used the WBD instrument on the four Cluster spacecraft to determine the locations of thousands of individual 'elementary radiation sources' (ERS) of AKR emission [26,*27*] using very long baseline interferometry (VLBI). The technique involves cross-correlating the waveforms from each of six pairs of spacecraft and measuring the differential delays at maximum correlation (Fig. 12).

This technique has several important advantages over previous AKR location studies: *(1)* It allows simultaneous determination of the locations of a large number of individual ERS sources at each frequency (3-axis phasing studies effectively determine the mean position of the integrated waveform); *(2)* It allows investigations of the motion and behaviour of individual ERS sources over time, since we analyze each ERS with very high time and frequency resolution, (3) the technique is intrinsically more accurate, providing positional uncertainties of 300-600 km when mapped to the auroral zone, compared with several thousand km uncertainties [e.g. 29] for 3-axis antenna measurements, and *(4)* it requires no assumptions about the polarization state of the AKR burst (phasing systems tacitly assume 100% circularly polarized [29]). This is expected for R-X mode, but a fraction of AKR is L-O mode [19], so that the net radiation may be only partially polarized.

Mutel et al. [26] demonstrated that AKR sources lie predominantly over the evening sector (20-24 MLT), but that they tend to occur in clumps that occupy only a small fraction of the auroral oval at any given time. Occasionally, clumps that have been tracked for spans of an hour or more have been observed to migrate in magnetic local time and/or invariant latitude, with speeds of near ~100 m/s.
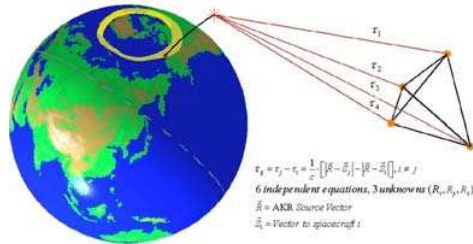
Fig. 12. WBD-VLBI location finding scheme using measured differential time delays.

2.3 Contemporaneous AKR Location studies with Auroral UV Imaging: The Magnetospheric-Ionospheric Connection

Starting in June 2004, we have begun a systematic joint study of AKR source locations using the VLBI differential delay location technique with contemporaneous UV imaging of the auroral oval with the FUV camera [22] on the IMAGE spacecraft. We are scheduling 2-4 observing epochs per month, each lasting 1-4 hours, depending on availability of downlink antennas for the WBD data. During these observations, both the Cluster and IMAGE spacecraft are co-located high above the same hemisphere.

An illustrative early result of these collaborative observations is shown in Figure 13. The observations were made on June 8, 2004 between 11:30-11:36 UT. Each IMAGE UV image is spaced at approximately two minute intervals, while the WBD AKR maps can be created on any timescale. During these observations, we switched frequencies at 52s and 104s intervals and made frequency-specific maps for each interval. In comparing the pairs of maps (which are nearly, but not quite concurrent), it is clear that there is in very good agreement between AKR burst locations and bright points in the auroral oval. However, not all bright points have associated AKR sources, and conversely, not all AKR sources are associated with distinct features in the auroral images. Benson and Akasofu [2] found a similar lack of correlation for some features, which could have been a result of incomplete auroral zone coverage, since the Alaskan ground network covered only a small fraction of the complete auroral oval.

We are now analyzing joint-epoch observations with higher time resolution and within a single frequency band, so that we can compare AKR locations using arbitrary time windows. The results from these studies will be published shortly.
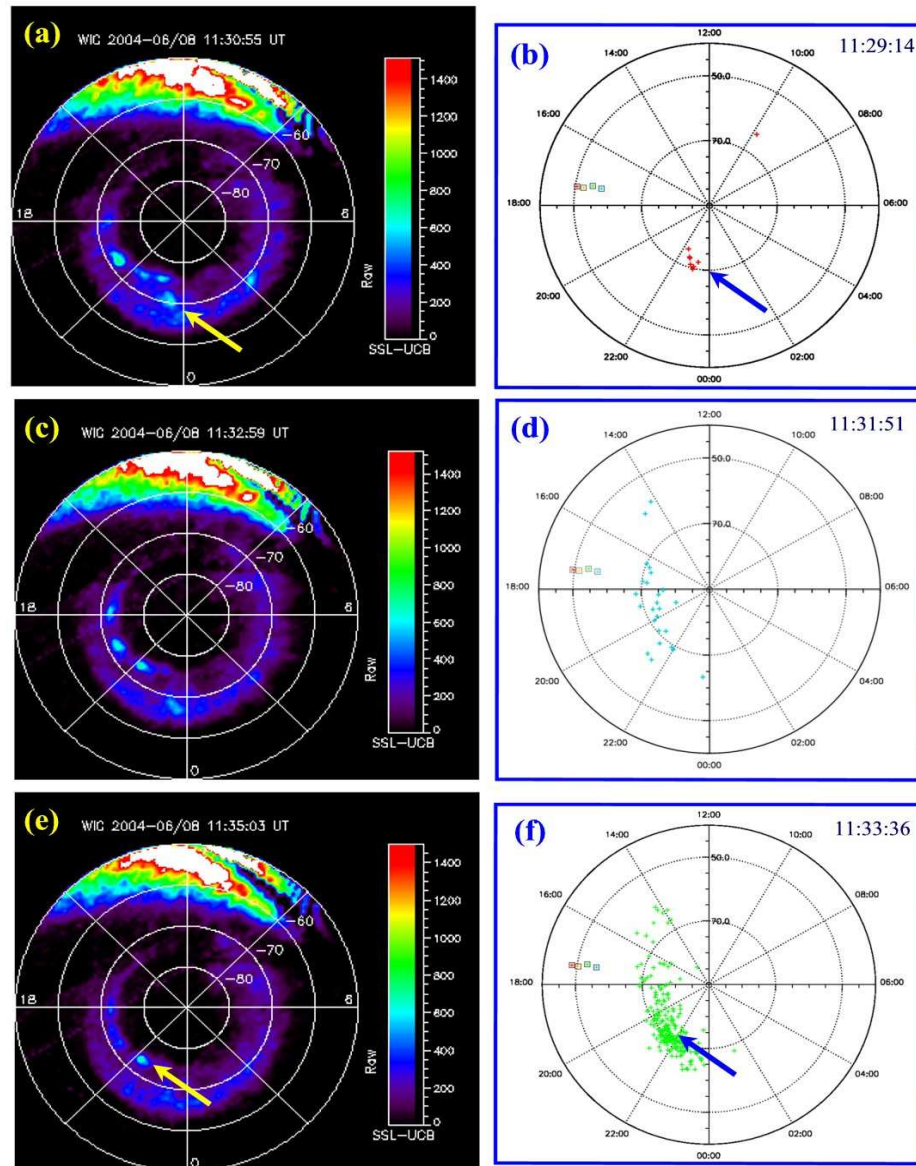
Figure 13. Comparison of UV auroral imaging on June 8, 2004 from IMAGE (left panels) with nearly simultaneous AKR imaging using the WBD VLBI technique on Cluster (right panels). Exposure times for each image are (a) 11:30:55 UT, (b) 11:29:14 UT, (c) 11:32:59 UT, (d) 11:31:51 UT, (e) 11:35:03 UT, and (f) 11:33:36 UT. Note the close position coincidence between optical and radio bright points as indicated by arrows in (a) – (b) and (e) – (f) image pairs.

ACKNOWLEDGEMENTS

REFERENCES

1. Baumback, M. and Calvert, W., The Minimum Bandwidths of AKR, *Geophys. Res. Lett.*, Vol. 14, 119-122, 1987.

2. Benson, R. F. and S-I. Akasofu, Auroral Kilometric Radiation/Aurora Correlation, *Radio Sci.*, 19,2, 527-541, 1984.

3. Bounds S. R., et al. Solitary Structures Associated with Ion and Electron Beams near 1 Re Altitude, *J. Geophys. Res.*, vol. 104, A12, 28709-28717, 1999.

4. Calvert, W., DE-1 Measurements of AKR wave directions, *Geophys. Res. Lett.*, 12, 6, 381-384, 1985.

5. Cattell, C. et al., Large amplitude solitary waves in and near the Earth's magnetosphere, magnetopause, and bow shock: Polar and Cluster observations, *Nonlin. Proc. Geophys.*, 10, 13-26, 2003.

6. Crumley, J, C. Cattell, R. Lysak, and J. Dombeck, Studies of ion solitary waves using simulations including hydrogen and oxygen beams, *J. Geophys. Res.*, 106, A4, 6007-6015, 2001.

7. De Lory G. T., et al. FAST Observations of Electron Distributions Within AKR Source Regions, *Geophys. Res. Lett.* Vol. 25, 12, 2069-2072, 1998.

8. Dombeck, J., e al. 2001, Observed trends in auroral zone ion mode solitary wave structure characteristics using data from Polar, *J. Geophys. Res.*, 106, A9, 19013-19021, 2001.

9. Ergun R. E., et al., FAST Satellite Wave Observations in the AKR Source Region, *Geophys. Res. Lett.*, Vol. 25, 12, 2061-2064, 1998.

10. Ergun, R., et al., FAST satellite observations of large-amplitude solitary structures, *J. Geophys. Res.*, vol. 25, 12, 2041-2044, 1998.

11. Ergun, R. E., et al., Electron-Cyclotron Maser Driven by Charge-Particle Acceleration From Magnetic Field-Aligned Electric Fields, *Astrophys. J.*, vol. 538, 456-466, 2000.

12. Goldman, M., et al., Phase-space holes due to accelerated electrons and ion beams accelerated by a current-driven potential ramp, *Nonlin. Proc. Geophys.*, 10:37-44, 2003.

13. Green J. L. and Gallagher, D. L., The Detailed Intensity Distribution of the AKR Emission Cone, *J. Geophys. Res.,* Vol. 90, A10, 9641-9649, 1985.

14. Gurnett, D., The Earth as a Radio Source: Terrestrial Kilometric Radiation, *J. Geophys. Res.*, Vol. 79, 28, 4227-4238, 1974.

15. Gurnett, D. et al., Initial Results form the ISEE-1 and 2 Plasma Wave Investigations, *Space Sci. Rev.*, Vol. 23, 103, 1979.

16. Gurnett, D, R. Huff, and D. Kirchner, The wide-band plasma wave investigation, Space Sci. Rev., 79, 195-208, 1997.

17. Huff, R. et al., Mapping of AKR Sources to the Aurora, *J. Geophys. Re*s., vol. 93, A10, 11445-11454, 1998.

18. Kurth, W., M. Baumback, and D. Gurnett, Direction-Finding Measurements of Auroral Kilometric Radiation, *J. Geophys. Res.*, 80, 19, 2764-2770, 1975.

19. Kumamoto, A. and H. Oya, Asymmetry of Occurrence Frequency and Intensity of AKR between summer polar region and winter polar region, *Geophys. Res. Lett*. Vol. 25, 2369-2373, 1998.

20. McFadden J. P., et al., FAST Observations of Ion Solitary Waves, *J. Geophys. Res*., Vol. 108, A4, 8018, 2003.

21. Melrose, D., A phase-bunching Mechanism for Frequency Fine-structure of AKR and Jovian Decametric Emission, *J. Geophys. Res.*, Vol. 91, 7970, 1986.

22. Mende, S. B., et al., Far ultraviolet imaging from the IMAGE spacecraft, *Space Sci. Rev*., 91, 287, 2000.

23. Menietti D. et al., Discrete, Stimulated AKR Observed in the Galileo and DE 1 wideband Data, *J. Geophys. Res.* Vol. 101, A5, 10673-10680, 1996.

24. Menietti, D., Persoon, A., Pickett, J., and Gurnett, D., Statistical Studies of AKR fine Structure Striations Observed by Polar, *J. Geophys. Res.,* Vol. 105, A8, 18857-18866, 2000.

25. Muschietti, L. et al., Modelling stretched solitary waves along magnetic field lines, *Nonlin. Proc. Geophys*., 9, 101, 2002.

26. Mutel R., et al., Locations of AKR Bursts Inferred from Multi-spacecraft Wideband Cluster VLBI Observations 1: Description of Technique and Initial Results, J. Geophys. Res., Vol. 108, A11, doi:10.1029/2003JA010011, 2003.

27. Mutel, R., Gurnett, D. A., and Christopher, I.W., Spatial and Temporal Properties of AKR Burst Emission Derived from Cluster WBD VLBI

Studies, Ann. Geophys., Vol. 22, 7, 2625-2632, 2004.

28. Omidi N. and Gurnett, D. A., Growth Rate Calculations of Auroral Kilometric Radiation Using the Relativistic Resonance Condition, *J. Geophys., Res.,* Vol. 87, A4, 2377, 1982.

29. Panchenko, M., Direction finding of AKR sources with three orthogonal antennas, *Radio Sci.*, 38, 6, doi:10.1029/2003RS002929, 2003..

30. Parrott, M., et al., Propagation Characteristics of Auroral Kilometric Radiation Observed by the MEMO Experiment on Interball 2, *J. Geophys. Res.*, Vol. 106, A1, 315-325, 2001.

31. Pederson, B., et al., Auroral kilometric radiation from transpolar arcs, *J. Geophys. Res.*, 97, A7, 10567-10573, 1992.

32. Pickett, J. et al., Solitary waves observed in the auroral zone: the Cluster multi-spacecraft perspective, *Nonlin. Proc. Geophys.,* 11:183-196, 2004.

33. Pottelette, R., R. Treumann, and M. Berthomier, Auroral Plasma Turbulence and the cause of the AKR fine structure, *J. Geophys. Res.* 106, A5, 8465-8476, 2001.

34. Pottelette R., Treumann, R. A., Berthomier, M., and Jaspers, J., Electrostatic Shock Properties Inferred from AKR Fine Structure, *Non. Proc. Geophys*, Vol. 10, 87-92, 2003.

35. Pottelette R. and Treumann R. A., Electron Holes in the Auroral Upward Current Region, *Geophys. Res. Lett.* , Vol. 32, L12104, 2005.

36. Pritchett P. L., et al., Free Energy Sources and Frequency Bandwidth for the Auroral Kilometric Radiation, *J. Geophys. Res.*, Vol. 104, A5, 10317-10326, 1999.

37. Roux A. et al., Auroral Kilometric Radiation Sources: In Situ and remote Observations From Viking, *J. Geophys. Res.*, Vol. 98, A7, 11657-11670, 1993.

38. Schreiber, R. et al., Auroral kilometric radiation source characteristics using ray tracing techniques, *J. Geophys. Res.,* 107, A11, 1381, doi:10.1029/2001JA009061, 2002.

39. Strangeway, R. J. et al., Accelerated Electrons as the Source of AKR, *Phys. Chem. Earth (C),* 26, 145-149, 2001.

40. Temerin, M. et al. , Observations of double layers and solitary waves in auroral plasmas, *Phys. Rev. Lett.,* 48, 1175, 1982.

41. Wu, C.S. and Lee, L. C., A Theory of the Terrestrial Kilometric Radiation, *Astrophys. J.*, Vol. 230, 621-626, 1979.

42. Yoon, P. and A. Weatherwax, A theory for AKR fine structure, *Geophys. Res. Lett*., 25, 24, 4461-4464, 1998.